RESEARCH METHODS

Molecular imaging of tumor metabolism: Insight from pyruvate- and glucose-based deuterium MRI studies

Elton T. Montrazi[1], Keren Sasson[2], Lilach Agemy[2], Avigdor Scherz[2], Lucio Frydman[1]*

Cancer diagnosis by metabolic MRI proposes to follow the fate of glycolytic precursors such as pyruvate or glucose, and their in vivo conversion into lactate. This study compares the ^{2}H MRI outlooks afforded by these metabolites when targeting a pancreatic cancer model. Exogenously injected [3,3′,3″-$^{2}H_3$]-pyruvate was visible only briefly; it generated a deuterated lactate signal throughout the body that faded after ~5 min, showing a minor concentration bias at the rims of the tumors. [6,6′-$^{2}H_2$]-glucose by contrast originated a lactate signal that localized clearly within the tumors, persisting for over an hour. Investigations alternating deuterated and nondeuterated glucose injections revealed correlations between the lactate generation and the glucose available at the tumor, evidencing a continuous and avid glucose consumption generating well-localized lactate signatures as driven by the Warburg effect. This is by contrast to the transient and more promiscuous pyruvate-to-lactate transformation, which seemed subject to transporter and kinetics effects. The consequences of these observations within metabolic MRI are briefly discussed.

INTRODUCTION

By detecting an increase in glucose uptake, molecular imaging modalities like positron emission tomography (PET) have become key players in the fight against cancer (*1*). In these scans, PET usually operates on the basis of the injection of a positron-emitting analog of glucose, which is avidly taken up by tumors having a sufficient perfusion. This reflects an up-regulated glucose metabolism, which coupled to the preferred production of lactate even in the presence of aerobic conditions that are hallmarks of the so-called Warburg effect (*2*, *3*). Stimulated by PET's success but also in view of PET's limitations and its inability to unambiguously stage a variety of cancers, recent years have seen extensive efforts to create alternative molecular imaging cancer diagnosis options based on magnetic resonance imaging (MRI) (*4*). Most remarkable among these are approaches that, based on dissolution dynamic nuclear polarization (dDNP), have enabled the in vivo MRI mapping of glycolytic fluxes (*5*, *6*). dDNP relies on the injection of hyperpolarized [1-$^{13}C_1$-pyruvate] and then monitoring its conversion to lactate, alanine, and other hyperpolarized metabolites that report on normal and abnormal pathway activities. These metabolites can be distinguished and imaged individually by ^{13}C magnetic resonance spectroscopic imaging (MRSI) (*7*, *8*); dDNP has led to several clinical trials (*6*, *8*–*10*), whose efforts have been recently complemented by the execution of similar experiments based on para-hydrogen–driven hyperpolarization (*11*). Regardless of how it is generated, the metabolic fate of hyperpolarized [1-$^{13}C_1$-pyruvate] can only be visualized over ~1 min, as after this time the hyperpolarization is lost and sensitivity becomes insufficient. This limits the achievable in-plane spatial resolution of the ensuing images; numerous biological transport and metabolic processes taking longer than a couple of minutes are simply outside the realm of this modality. Alternative routes to map cancer-related metabolic changes by MRI rely on following the fate of glucose itself under conventional, thermal polarization. Chemical exchange saturation transfer (CEST) MRI of glucose ("glucoCEST") offers a route of doing so: While unable to monitor metabolic products, glucoCEST imparts information about glucose's local concentration onto surrounding waters, which can then be used to acquire quality high-resolution MR images mapping the glucose distribution (*12*, *13*). Still, the spectral proximity between the glucose and the water resonances have limited the scope of such studies—particularly if aimed at organs outside the brain, subject to motion and susceptibility broadenings. Alternatively, MRI experiments targeting the hydrogen isotope deuterium, ^{2}H, have also been recently proposed as potential reporters of metabolism (*14*). In these deuterium metabolic imaging (DMI) experiments, [6,6′-$^{2}H_2$]-glucose is administered, and both its uptake and its resulting deuterated products are mapped by ^{2}H MRSI. In particular, it was observed that, if selectively enriched glucose is administered, it will convert into [3,3′-$^{2}H_2$]-lactate in tumors as a reflection of the Warburg effect, into ^{2}H-water (HDO) as a metabolic end-product of a variety of pathways, and, in brain, into deuterated glutamate species (*15*–*18*).

A unique opportunity presented by deuterated species as metabolic imaging reporters is their ability to probe the fate of different biomolecules—both for enhancing our understanding of organ- and tumor-specific metabolic fluxes and to enhance MRSI's diagnostic potential. The present study exploits this opportunity by comparing the pictures that ^{2}H MRSI provides, on the same pancreatic cancer model, upon examination using glucose and pyruvate as initial substrates. This tumor model was here chosen because of the dire need to perfect methods for the early detection of pancreatic ductal adenocarcinoma (PDAC), which is now the third most common cause of cancer-related deaths and is predicted to become the number one cause by the end of the decade (*19*, *20*). PDAC's lethalness is largely due to the difficulties arising in imaging and diagnosing this disease before it has metastasized (*21*). Recently, it has been shown for different PDAC cases that both hyperpolarized ^{13}C MRSI (*22*–*24*) and glucose-based DMI approaches (*25*, *26*) could provide indication about the presence of these tumors, via the generation of lactate. In the former case, an increase in the ratio between hyperpolarized lactate/pyruvate was detected preferentially at the tumors, while in the latter case, the presence of deuterated lactate in the tumor could be clearly ascertained following the [6,6′-$^{2}H_2$]-glucose injection. In addition to different

[1]Department of Chemical and Biological Physics, Weizmann Institute of Science, Rehovot, Israel. [2]Department of Plant and Environmental Sciences, Weizmann Institute of Science, Rehovot, Israel.
*Corresponding author. Email: lucio.frydman@weizmann.ac.il

timescales, differences arose between the two approaches when trying to distinguish pancreatic tumors from pancreatitis (*27*)—with deuterated glucose providing a more accurate differential identification. The present study attempts to further understand these differences, both from the standpoint of the metabolic dynamics that they reflect and of their potential use in cancer diagnosis. To this effect, the pictures that injections of deuterated pyruvate and deuterated glucose provide for the same type of PDAC tumor were examined by ^{2}H MRSI at 15.2 T. These experiments were complemented by alternated injections of the deuterated and protonated precursors at different dosages, which revealed both different specificities for the two kinds of metabolic probes and different spatiotemporal patterns for the biosynthesis of their deuterated products. In unison, these experiments present a consistent picture about the different metabolic processes reflected by glucose and pyruvate when used as molecular imaging agents, and on the different usefulness that these two probes may have in diagnosing and prognosing pancreatic cancer and tumors in general.

RESULTS

Glucose versus pyruvate: The ^{2}H MRSI outlook

Figure 1 summarizes prototypical results obtained upon investigating the generation of deuterated lactate and HDO, following the injection of deuterated pyruvate (Fig. 1, A to C) and of deuterated glucose (Fig. 1, D to F). For each case, the panels present an anatomical ^{1}H image highlighting the tumor of these PDAC-implanted animals, a series of nonlocalized ^{2}H NMR spectra and of metabolic ^{2}H maps collected for the various metabolites as a function of post-injection times, and the metabolic concentrations computed over these times using the initial intensity of natural abundance HDO [as well as the sequence parameters (*26*)] as internal concentration reference. All plots are depicted for regions of interest (ROIs) centered on the tumor and on a kidney used as reference of healthy tissue; all these data are shown after performing a subtraction of the fat signal, which in these abdominal studies will otherwise provide a broad contribution centered at ~1.1 parts per million (ppm); see section S1.

The nonlocalized spectra in Fig. 1B reveal that the injected pyruvate is immediately converted into lactate and HDO. Before the [3,3′,3″-^{2}H$_3$]-pyruvate injection, only the natural abundance HDO peak is present in the fat-suppressed spectra; 30 s after the pyruvate injection, the ^{2}H spectrum shows an increase in this HDO peak, along with the appearance of peaks at 2.2 and 1.2 ppm. Even at these short times, the lactate peak is already higher than the pyruvate peak, reflecting the high rate at which pyruvate is converted in vivo into lactate. Both peaks have already disappeared from the NMR spectrum by the time the first of the ^{2}H MRSI acquisitions has completed, ~6 min post-injection. The intensity of the [3,3′,3″-^{2}H$_3$]-pyruvate is too low, and its rate of consumption is too fast to be scanned with sufficient sensitivity by our MRI setup. Deuterated water is also rapidly generated, increasing ~50% from its initial natural abundance value within the first image acquisition and staying at a steady level thereafter. Lactate also increases transiently, presenting both spectroscopic and imaging patterns that are very similar to those observed on healthy control animals (see section S2 and fig. S4). In the sole ^{2}H image that chemical shift imaging–steady-state free precession (CSI–SSFP) MRSI captures for the lactate peak, this metabolite appears at first randomly distributed throughout the sensitivity region captured by the ^{2}H surface coil. Despite this apparent lack of specificity, distinctions begin to emerge when data processing includes fat subtraction. These highlights are easiest to appreciate when considering the one-dimensional (1D) ^{2}H NMR spectra (e.g., Fig. 1B versus section S1 and fig. S2), but they are also observed in the 2D ^{2}H MRSI images. Fat suppression reveals the presence of a "ring" of lactate forming around the tumor region. This is a noisy pattern, but it was observed, consistently, in nearly all the [3,3′,3″-^{2}H$_3$]-pyruvate injection experiments that were performed on the different animals (see, for instance, figs. S3 and S5). Note that none of our experiments evidenced a peak at 1.4 to 1.5 ppm, which could have been ascribed to deuterated alanine—an alternative byproduct of pyruvate via transamination (*28*).

By contrast to pyruvate's behavior, when [6,6′-^{2}H$_2$]-glucose was administered, this precursor could be observed throughout the body for more than 1 hour. This injected glucose eventually becomes preferentially located in a rim surrounding the tumor region (Fig. 1D; see also section S5). The injected glucose is consumed slowly compared to the pyruvate, and its disapparition is accompanied by a concurrent increase in the HDO signal intensity, which extends over several hours. At first sight, the ^{2}H images seem to suggest an enhanced concentration of this metabolically generated HDO in the tumor region; however, upon accounting for the different relaxation times in the tumor and nontumor regions (the tumor having longer T_2s than healthy tissues, which ends up biasing up the SSFP signal intensity), these differences revealed only a limited statistical significance: The $\frac{[\mathrm{HDO}]_{\mathrm{tumor}}}{[\mathrm{HDO}]_{\mathrm{kidney}}}$ ratio over $n = 8$ analyzed animals was 1.3 ± 0.2. The glucose-derived lactate signal is often hard to observe in the nonlocalized ^{2}H NMR spectra, which are signal averaged for only 30 s; in the longer times that it takes to collect the metabolic maps, however, lactate signals clearly show up and exclusively appears inside the tumor region. This agrees with the extensive data in (*25*–*27*). Although pyruvate is present in the metabolic pathway leading from glucose to lactate, its signature peak does not appear in either the MRSI images nor the nonlocalized ^{2}H spectra; this probably reflects, once again, the short lifetime and low concentration achieved by the deuterated pyruvate arising from the glucose injection.

As the differences between the ^{2}H MRSI reflected by the pyruvate and glucose injections shown in Fig. 1 could also reflect the fact that these experiments were run on different animals, biological variability was assessed by conducting the experiments on the same animal. To this end, a PDAC-implanted mouse was tail vein cannulated, injected initially with a dose of [3,3′,3″-^{2}H$_3$]-pyruvate and, subsequently, with a dose of [6,6′-^{2}H$_2$]-glucose. Figure 2 summarizes the results from such experiment, which are essentially the same to those that were revealed in Fig. 1 on two different animals: No initial pyruvate signal could be captured by the metabolic maps, which did however reveal the formation of deuterated lactate throughout the body. Despite this relatively uniform spread, a ring of pyruvate-derived lactate could still be discerned forming in the periphery of the tumor upon fat subtraction; this deuterated lactate decayed back to baseline levels after ~10 min. Pyruvate's rapid catabolism is also reflected in a rapid increase of the HDO concentration, which remains steady after the first couple of images. Thereafter, when [6,6′-^{2}H$_2$]-glucose is injected, the results exhibit a behavior that is very much akin to that shown in Fig. 1B. Also, in this case, glucose remained throughout the body for an extended period, including an initial accumulation in the kidney and eventually an enhanced concentration on a rim around the tumor. A lactate ^{2}H signal appeared inside the tumor reaching its peak ~45 min after the glucose injection, having a spatial distribution that is distinctly

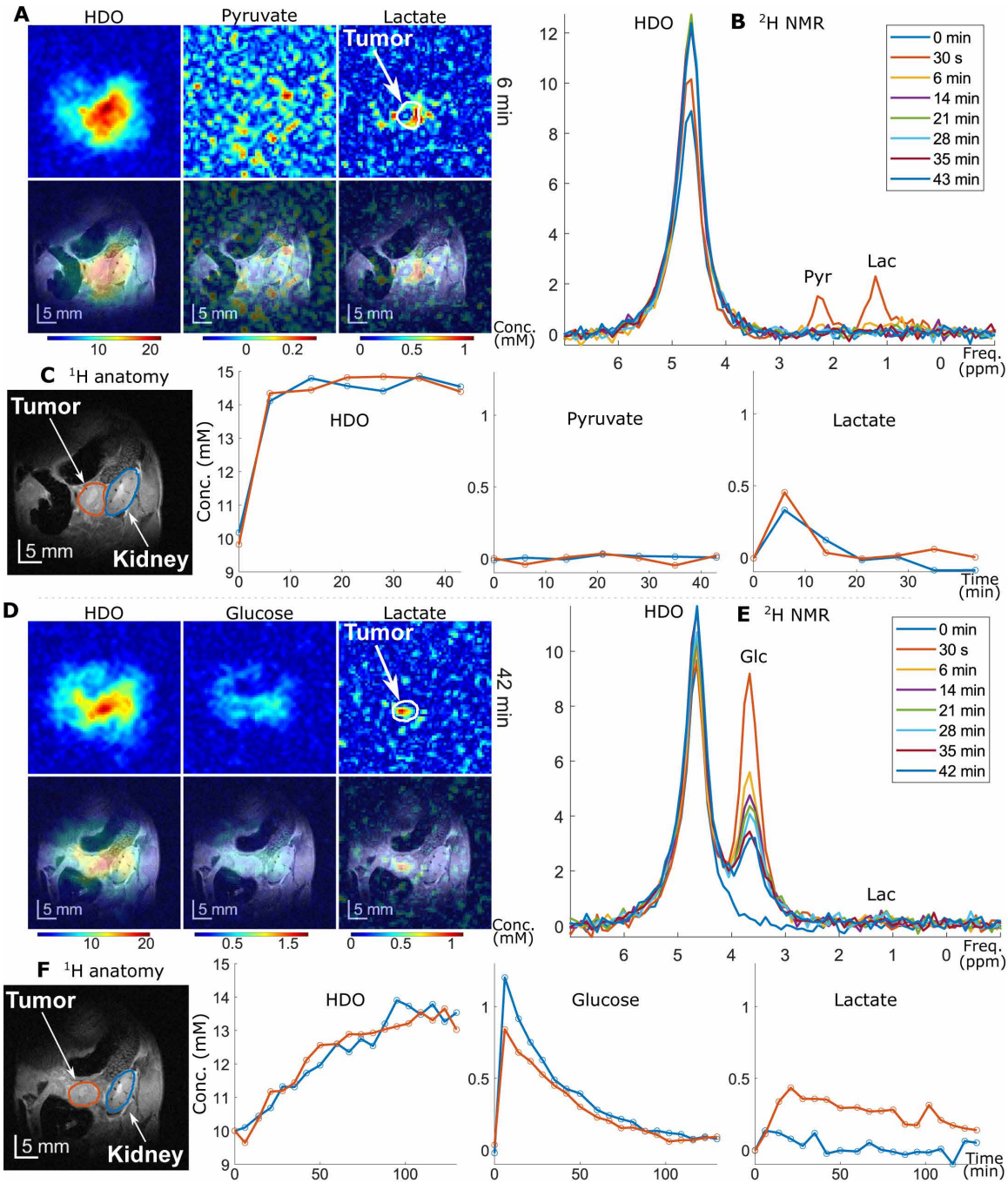

Fig. 1. Summary of the ^{2}H MR results obtained upon injecting into PDAC-implanted mice. (**A** to **C**) With [3,3′,3″-$^2H_3$]-pyruvate. (**D** to **F**) With [6,6′-$^2H_2$]-glucose. Shown in the top left of each dataset [(A) and (D)] are the metabolic maps for HDO, pyruvate/glucose, and lactate resolved by CSI-SSFP, for the indicated post-injection times (6 and 42 min, respectively). All these ^{2}H images are also shown overlaid on the ^{1}H anatomic images [(C) and (F)]. Shown to the right of each dataset [(B) and (E)] are nonlocalized ^{2}H NMR spectra collected at the displayed post-injection times. Graphs underneath these spectra depict the time-dependent metabolic concentrations obtained from the metabolic maps for tumor and kidney ROIs (indicated in the ^{1}H images), as resolved for each chemical shift. Concentrations are derived from the initial HDO map, as described in (*26*) and in Methods. The animals were fasted for 4 hours before the studies.

different from that arising from the [3,3′,3″-$^2H_3$]-pyruvate injection. All these changes are accompanied by a steady increase in the HDO concentration, which lasts for over two hours. No differences in the ^{2}H studies arising from the [3,3′,3″-$^2H_3$]-pyruvate or [6,6′-$^2H_2$]-glucose injections could be noticed regardless of whether animals were fed ad libitum or fasted 4 hours before the experiments (section S3).

The higher specificity with which [6,6′-$^2H_2$]-glucose reveals the presence of tumors could be reflecting several factors—including the loss of the pyruvate's deuterons by spontaneous exchanges with the water protons driven by keto-enol tautomerism or by transamination reactions, as well as the different concentrations used in the pyruvate vis-à-vis glucose injections. The latter values are limited by physiological

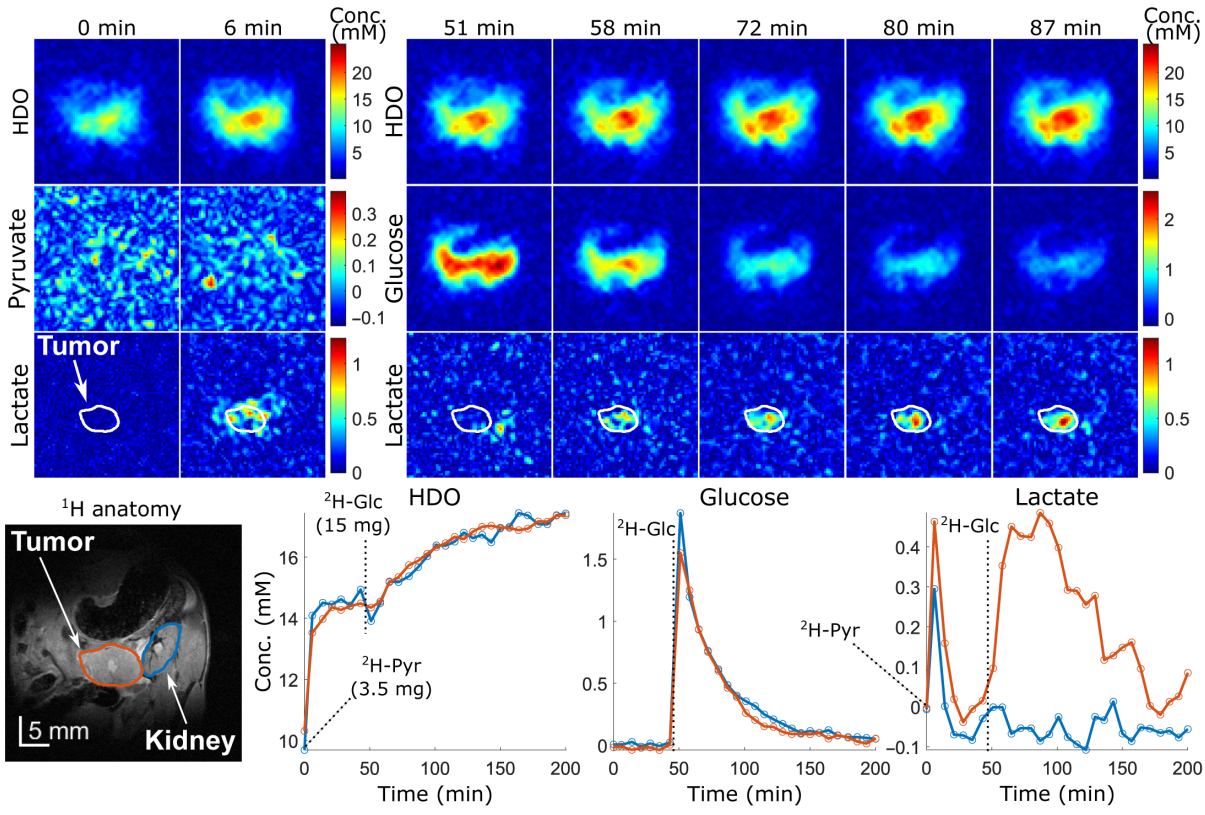

Fig. 2. Metabolic study based on subsequent deuterated pyruvate and glucose injections, executed on the same PDAC-implanted mouse. The tumor ROI is outlined by a white line in the colored ^{2}H MRSI maps (top); red and blue lines in the metabolic concentrations curves (bottom) correspond to tumor and kidney ROIs, as outlined in the ^{1}H anatomic image (grayscale). Also indicated by dashed lines were the times at which the deuterated pyruvate (3.5 mg) and the glucose (15 mg) were tail vein injected; each point in the metabolic curves is spaced ~6 min apart, and all concentrations are calibrated according to the pre-injection HDO intensity. Notice the small transient instability in the HDO signal upon administering the glucose; this was observed in ~50% of the animals analyzed and its origin is unclear. The mouse was fed ad libitum.

issues, as injections of concentrated pyruvate proved toxic to the animals. Still, an experiment was carried out whereby 0.5 ml of a 0.73 M [3,3′,3″-$^{2}H_3$]-pyruvate solution in phosphate-buffered saline (PBS) was infused over 5 min in a PDAC-implanted mouse. The animal survived this 40-mg sodium pyruvate injection, leading to higher in vivo concentrations of deuterated lactate and of HDO. However, little additional specificity was obtained from this higher concentration experiment, in connection to highlighting the tumor itself (fig. S6). Additional potential factors that could rob the pyruvate experiments from specificity, including the back-conversion of deuterated lactate into pyruvate and/or the creation of an additional intermediate from the [3,3′,3″-$^{2}H_3$]-lactate, were also explored; however, none of these processes was experimentally observed (section S4).

Warburg response as a function of glucose concentration

In addition to the different spatial distributions characterizing the lactate emanating from the deuterated pyruvate and glucose injections—with the latter eliciting a more localized, tumor-specific lactate production—the most remarkable difference between the two sets of studies resides in the very different rates at which precursors are consumed and products are generated. When [3,3′,3″-$^{2}H_3$]-pyruvate is injected, it is swiftly metabolized, and deuterated lactate shows up for ~5 to 10 min before it becomes invisible; a similar rapid change happens in the HDO signal but none thereafter. Similarly, boluses of 130 mM [3,3′,3″-$^{2}H_3$]-lactate were metabolized in healthy animals within ~10 min after their injection (fig. S7). By contrast, the deuterated lactate signal remains long after the [6,6′-$^{2}H_2$]-glucose bolus has been injected, with a steady increase in the HDO signal intensity that extends for hours after the injection. The rapid disappearance of deuterated lactate—whether it has been infused (fig. S7) or been generated by the [3,3′,3″-$^{2}H_3$]-pyruvate—suggests that this metabolite is rapidly consumed and/or washed out. This in turn raises the question of why, once the [6,6′-$^{2}H_2$]-glucose resonance signal diminishes to barely detectable levels in the metabolic maps (≥90 min after the initial administration), the lactate signal does not similarly vanish. This is also connected to the question of what defines the detection limits for the deuterated glucose observed in these MRSI experiments. To investigate this further, the protocol presented in Fig. 3 was assayed. In it, a mouse (which in this case happened to have two metastases of the primary cancer, with all three tumors lying within the coil-targeted area) was injected with four different aliquots, while ^{2}H NMR and MRSI data were continuously recorded. The first injection was our standard [3,3′,3″-$^{2}H_3$]-pyruvate aliquot; [6,6′-$^{2}H_2$]-glucose at different concentrations (17, 40, and 60 mg, respectively) was subsequently injected every 3.5 hours. As before, the pyruvate injection led to lactate spreading evenly throughout the body, with a slight specificity in the peripheries of the metastatic tumors. Lactate had returned to baseline by the time the first of the [6,6′-$^{2}H_2$]-glucose injections was dispensed, which led to a steady increase in both the overall HDO signal, as well as in the deuterated lactate generated by all three PDAC tumors. This pattern was repeated, with increased

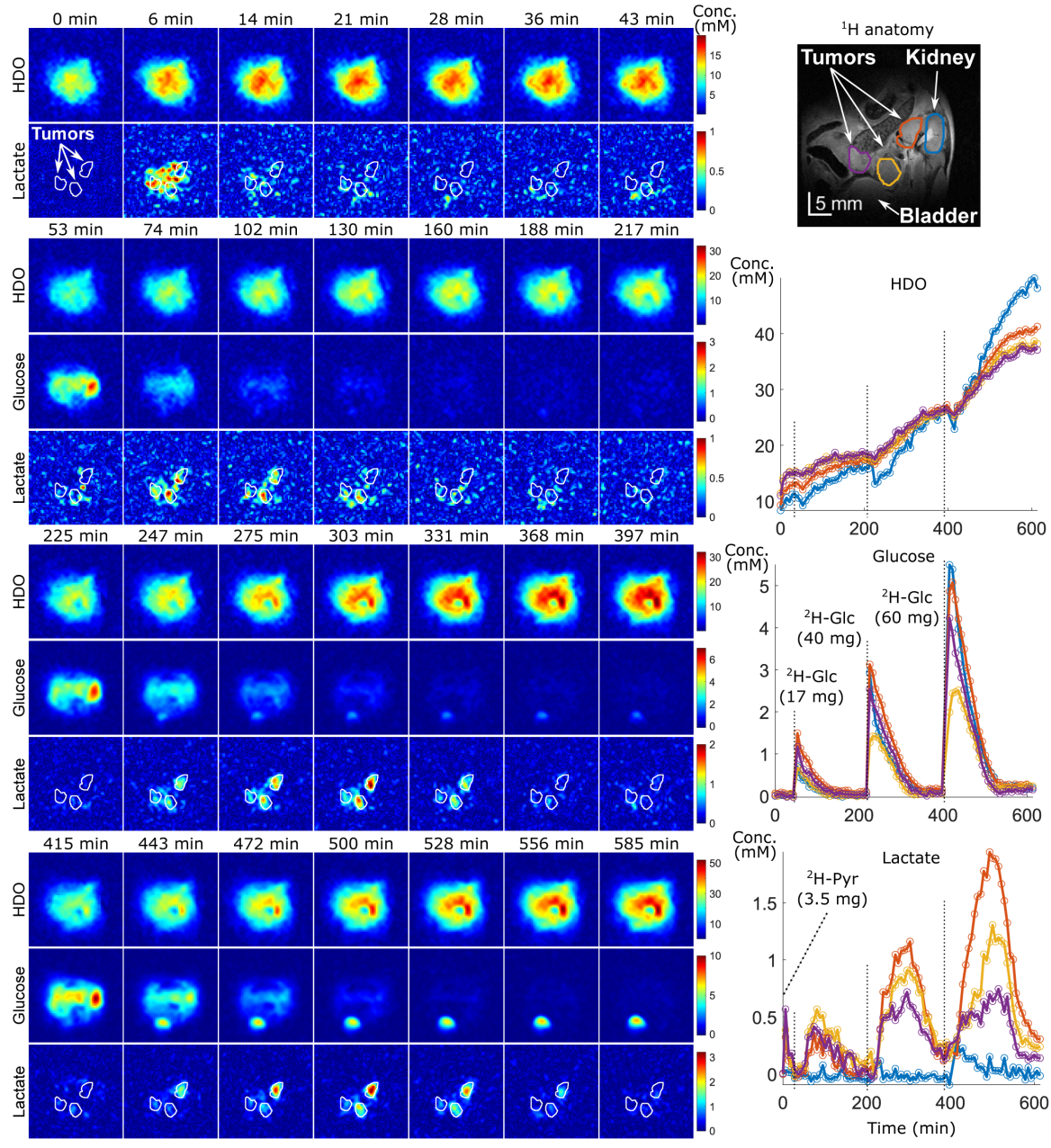

Fig. 3. Selected metabolic maps, plots of overall metabolic concentrations over time, and accompanying ^{1}H anatomic image, arising from experiments on a mouse having three PDAC tumors, subjected to different deuterated pyruvate and glucose injection protocols over the course of a 10-hour experiment. The colors (red, orange, purple, and blue) reflect signals arising from the corresponding regions marked on the ^{1}H anatomical image; dotted lines indicate the moments of the various injections. The concentration dependencies also indicate the timing and the amounts of glucose injected over the course of this experiment. Notice the different patterns evidenced by the deuterated lactate produced by the pyruvate and glucose injections, the different color maps accompanying each set of injections, as well as the growing amounts of lactate produced from increasing amounts of glucose injection: Only the tumor circled in purple exhibits some sort of "saturation" between the second and third injections.

intensity, each time that the [6,6′-$^{2}H_2$]-glucose dose was incremented. For one of the tumors lactate production appeared saturated after the 40-mg glucose injection, but for the other two tumors, the lactate concentration continued to grow every time that the increasing glucose doses were administered. Notice that in the last two [6,6′-$^{2}H_2$]-glucose injections, and particularly in the last one, the ability of the animal to assimilate the glucose is overwhelmed, as evidenced by an excess of [6,6′-$^{2}H_2$]-glucose spilling directly into the bladder. Notice as well that despite the increasing glucose doses, the lactate produced concentrates exclusively in the tumor regions. The conclusion is that the tumor never ceases to consume glucose and that lactate will be produced as long as glucose is available: The amount of generated lactate seems limited only by the amount of glucose available to the tumor.

Washout experiments confirm a continuous glucose consumption and rapid lactate turnover

Two conclusions arise from the aforementioned results. The [3,3′,3″-$^{2}H_3$]-pyruvate injections imply that once the originating substrate is

consumed, the deuterated lactate that had been generated will disappear rapidly from the system—either by consumption (fig. S7) or wash-out. As for the [6,6′-$^2H_2$]-glucose injections, their results suggest that as long as the tumor has this substrate available, it will continually use it to produce lactate. These two features combined suggest that the long timescales over which deuterated lactate is observed in the glucose-based DMI experiments reflect the underlying presence of deuterated glucose and/or of deuterated derivatives in the system. This hypothesis implies that if the [6,6′-$^2H_2$]-glucose or its deuterated derivatives could be suddenly removed from the body, the deuterated lactate signal would also rapidly disappear. While removing glucose from the body is not straightforward, it is to some extent possible to mimic the effects of such elimination, by following the administration of [6,6′-$^2H_2$]-glucose with a dose of nondeuterated (i.e., protonated) glucose: This "cold" precursor should displace the deuterated "hot" substrate and induce changes in the ^{2}H MRSI experiment. Figure 4 shows the results emerging from of such "hot/cold" chasing experiment, which included an initial injection of [3,3′,3″-$^2H_3$]-pyruvate, alternated with the administration of deuterated and protonated glucose doses. As before, the deuterated lactate originating from the [3,3′,3″-$^2H_3$]-pyruvate spreads throughout the body—with both the lactate and pyruvate signatures disappearing in a few minutes. As a 200-μl bolus containing [6,6′-$^2H_2$]-glucose (2 g/kg) is injected into the body, a clear concentration in the kidney arises, because of the relatively high dose used; progressively larger amounts of deuterated lactate also appear in the tumor. On the basis of the measurements previously described, this lactate signal would be expected to persist for over an hour; however, the injection of protonated (cold) glucose induces a sudden drop of this tumor ^{2}H-lactate signal, which disappears within a matter of minutes. Section S6 presents a similar experiment but without the initial [3,3′,3″-$^2H_3$]-pyruvate injection and using smaller doses of [6,6′-$^2H_2$]-glucose. The overall behavior shown in that additional dataset is like that in Fig. 4: The glucose uptake is eventually saturated, but the generation of deuterated lactate at the tumor site increases with every [6,6′-$^2H_2$]-glucose injection—until the cold, all-^{1}H-glucose, is applied. At this point, the tumor continues metabolizing glucose into lactate, but since the former is now protonated, the [6,6′-$^2H_2$]-glucose is displaced and the deuterated lactate signature drops rapidly. Notice as well that, immediately after the injection of the protonated glucose, there is a small but consistent increase in the [6,6′-$^2H_2$]-glucose signal visible in the kidney (Fig. 4 and fig. S9). We ascribe this to the fact that, as protonated glucose is injected and the overall glucose level throughout the animal's circulation system rises, the kidney proceeds to filter out the excess of glucose it already had (which was deuterated) and expel it as urine. An increase of deuterated glucose in the bladder upon injecting the ^{1}H-glucose is indeed also visible (e.g., final glucose images in fig. S9). Notice as well the distinct behavior of the HDO signal, which increases more or less steadily throughout the experiment both inside and outside the tumor.

DISCUSSION

The present study was elicited by the ability demonstrated by both pyruvate-based hyperpolarized ^{13}C MRSI and glucose-based ^{2}H MRSI experiments to highlight noninvasively the presence of metabolically active tumors. The question naturally arises on how these approaches compare. This work explored such aspect using a representative pancreatic cancer model, in a series of tests which substantiated very different characterization abilities for the two precursors. In agreement with what had been previously seen by hyperpolarized ^{13}C MRSI, ^{2}H MRSI experiments also evidenced the ability of the pyruvate ➔ lactate conversion process to highlight tumors. The rapid timescales revealed by ^{2}H MRSI for this metabolic process were also consistent with those observed by hyperpolarized MRSI. This conversion, however, had a relatively weak specificity: pyruvate converted into lactate throughout the animal body, with a relatively weak (≈twofold) bias toward a lactate enhancement in the periphery of the tumors. Most likely, given the relatively low resolution of our previous hyperpolarized ^{13}C MRSI experiments—~4 mm in-plane versus 1.25 mm in the present ^{2}H work—this led to the appearance of a high lactate/pyruvate ratio centered on the tumor region. While it is reasonable to assume that the details of this specificity and of the spatial distribution will depend on the tumor's characteristic, it is also clear that pyruvate will in general also be rapidly consumed and transformed into lactate and other metabolites by healthy tissues, thereby limiting its ensuing cancer reporting abilities based solely on changes in the lactate/pyruvate ratio. Moreover, the fast timescales of the pyruvate ➔ lactate conversion imply that—as was the case in hyperpolarized ^{13}C MRSI—also these ^{2}H experiments will be dominated by foremost by a transport kinetics dictated by monocarboxylate transporters, as well as by changes lactate dehydrogenase activities (*29*, *30*). By contrast, the generation of the lactate arising from deuterated glucose reflects overall changes in the glycolysis process (*31*, *32*) including, very clearly, the onset of the Warburg effect. This is reflected in the tumors' avidity to convert glucose into lactate and in a continuous increase in deuterated lactate observed upon performing multiple [6,6′-$^2H_2$]-glucose injections, evidencing how tumors will keep on consuming glucose with almost no sign of satiation. The ensuing generation of deuterated lactate ended up evidencing the PDAC-affected regions much more clearly than the uptake of glucose itself, which only showed an accumulation throughout the tumors' periphery. Such "rim effects" have also been noticed in PET analyses of certain cancers, when monitoring the uptake of fluorinated deoxy-glucose (FDG) (*33*–*35*); these rim effects were then ascribed to the presence of a necrotic center, where the administered FDG would not reach easily. However, while necrosis and/or cysts may be present in larger tumors, these were unlikely in our relatively small (≈3 to 5 mm in diameter) tumors, which also showed similar rim effects in their deuterated glucose images. In consequence, we are inclined to ascribe in these cases the drop of glucose within the tumor to an enhanced rate of glucose ➔ lactate conversion within the PDAC itself, hence rationalizing both the drop in the glucose concentration and the lactate enhancement resulting from the Warburg effect. Regardless of interpretations, it is clear that since glucose, like pyruvate, will be consumed more or less homogeneously by many metabolically active tissues, including the brain and tissues subject to inflammations, approaches that like PET rely solely on glucose uptake—as opposed to approaches that like DMI reflect glucose's metabolic products—will be limited in their ability to provide optimal molecular images of cancer.

Another aspect worth discussing is the steady increase in glucose-derived lactate, demonstrated by the DMI experiments. While lactate appears to increase for 45 to 60 min following the [6,6′-$^2H_2$]-glucose injections, both the pyruvate-based and the protonated glucose chasing experiments reveal that lactate's lifetime within the tumor is relatively short and is eliminated within just a few minutes. The long lifetimes that we observe for the deuterated

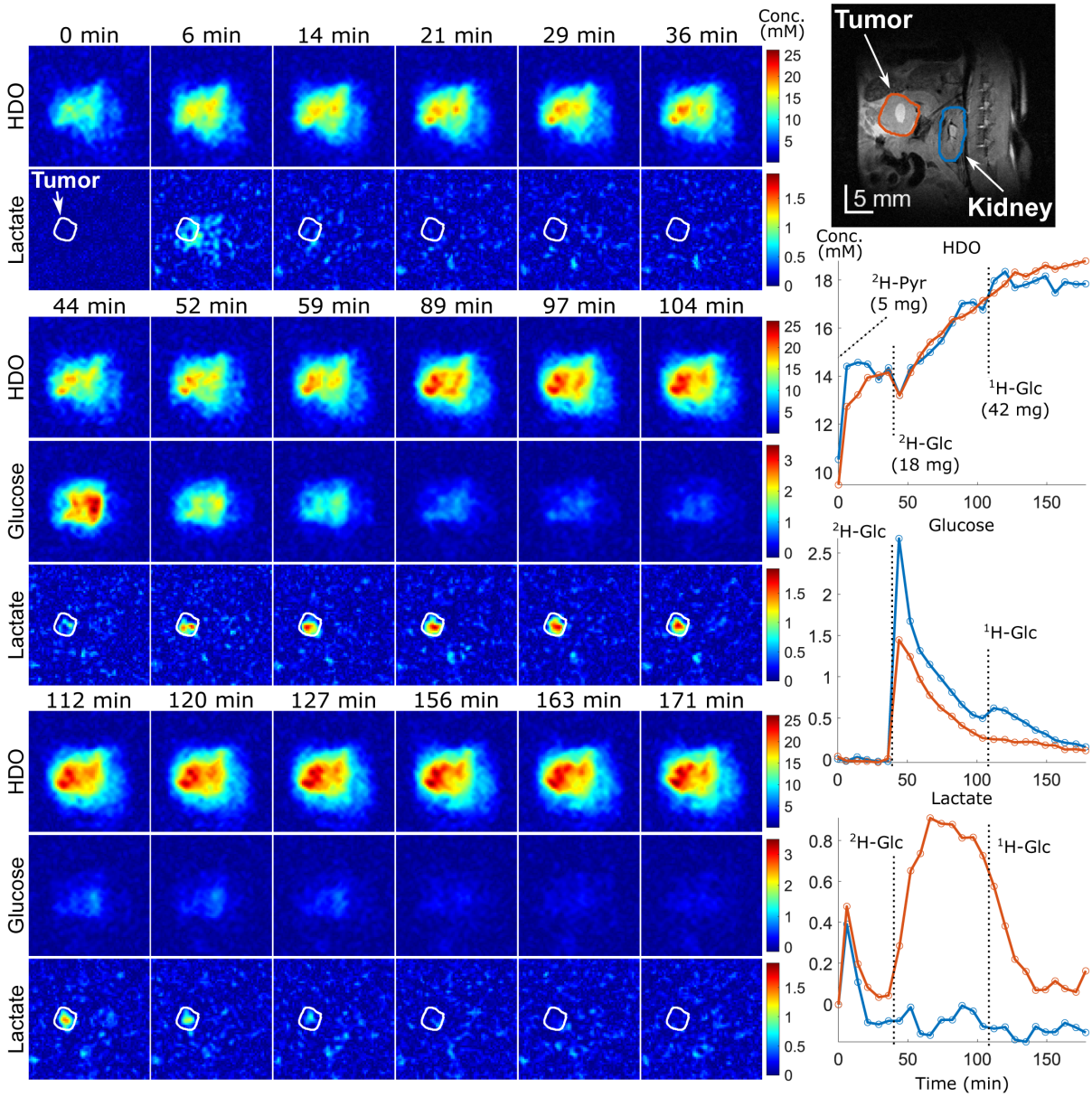

Fig. 4. Selected metabolic maps and metabolic time dependencies observed in deuterated/protonated pyruvate/glucose chasing studies performed on a PDAC-implanted animal fed ad libitum. After an initial 5-mg [3,3′,3″-$^2H_3$]-pyruvate injection, lactate is observed spreading throughout the body. A subsequent 18-mg [6,6′]-$^2H_2$-glucose injection elicits a clear lactate signal inside the tumor. After a 1-hour period, the injection of 42 mg of protonated glucose results in a rapid drop in the tumor's lactate and to a temporary increase in the deuterated glucose arising from the kidney. Dotted vertical lines indicate the instant at which the injections were made. See section S6 for a slightly different but consistent hot/cold chasing experiment.

lactate could in part reflect the higher glucose concentrations used in the ^2H MRSI experiments: 0.4 to 1 M versus. ~0.1 M for the deuterated pyruvate. Most likely, however, the long-lifetime behavior is also reflecting the different steady-state concentrations that will be present for pyruvate and glucose following the initial bolus injection: Pyruvate is an important intermediate in several metabolic pathways, and as such, its concentration at any given time is relatively low (~0.1 mM). Glucose by contrast is a precursor that is present at ~10-fold higher concentrations, and hence, its longer lifetime throughout the circulatory system is understandable. This also helps understand: (i) the relative independence of the observed results on whether the animals were administered the [6,6′-$^2H_2$]-glucose in the presence or absence of fasting; (ii) our previous failure to notice any differences in the buildup of deuterated lactate, depending on whether the glucose was injected all at once or in aliquots distributed over several minutes (*36*); and (iii) the HDO signal behavior, which is seen to grow in these experiments throughout several hours after the [6,6′-$^2H_2$]-glucose injections.

In summary, the present study demonstrated the superior ability of glucose-based ^2H MRSI experiments to highlight the presence of

pancreatic tumors on animals vis-à-vis pyruvate-based counterparts, thanks to the particular metabolic information that these measurements carry. The translation of these experiments and insight onto humans and the unraveling of their information into fluxes capable of serving biological, prognostic, and diagnostic purposes are in progress.

METHODS

[3,3′,3″-$^2H_3$]-pyruvate preparation

Pyruvic acid (2 g, 22.7 mmol) was dissolved in D_2O (85 ml) and heated to 95°C under N_2 for 20.5 hours. After this time, the mixture was allowed to cool down to room temperature, and sodium bicarbonate (1.81 g, 21.9 mmol, 0.95 eq.) was added. The solvent was evaporated at reduced pressure using a water bath at 40°C. The remaining solid was recrystallized from D_2O (10 ml) and absolute ethanol (EtOH; 120 ml). The white sodium pyruvate crystals were collected by filtration, washed with absolute EtOH, and dried under vacuum (1.57 g, 77%). The mass spectrum of the solid showed that it contained 87% of the $-CD_3$ species, with the remaining being mostly CD_2H pyruvate. A 1D ^2H NMR spectrum of the sodium salt revealed a minor peak at ~1.3 ppm, which we ascribe to pyruvate's dimerization and which, according to its intensity, amounted to a ~3% fraction.

In vivo conditions

In vivo experiments were approved by the Weizmann Institute Institutional Animal Care and Use Committee, accredited by the Association for Assessment and Accreditation of Laboratory Animal Care, the US National Institutes of Health Office of Laboratory Animal Welfare, and the Israel Ministry of Health. All methods and procedures were performed in accordance to relevant guidelines and regulations. This study is reported in accordance with ARRIVE (Animal Research: Reporting of In Vivo Experiments) guidelines. In these experiments, 13 C57 black mice were implanted with KPC rodent PDAC and examined approximately 10 days after implantation. KPC is a genetically engineered mouse cancer having key genetic similarities with human PDACs, which have made it a common model for drug discovery purposes (*37*). Three C57 black mice were used as controls for the pyruvate study. Enriched [6,6′-$^2H_2$]-glucose was purchased from Cortecnet, Voisins-le-Bretonneux, France.

Injections of pyruvate and of glucose were administered, as often done in hyperpolarized studies, as single boluses of ~250 μl. Approximately 3.5 mg for mice weighting approximately 20 g of deuterated sodium pyruvate in Dulbecco's PBS (~120 mM PBS solutions) was used for these experiments. This concentration was chosen on the basis of the similar dosing that is used in hyperpolarized [1-$^{13}C_1$]-pyruvate experiments (*23*, *38*). Deuterated glucose injections were carried out using ~0.7 to 2.8 g of glucose per kg of animal body weight (~0.37 to 1.48 M solution in PBS) as specified below; these concentrations were chosen on the basis of similar concentrations used in the glucose tolerance test [~100 ml of a 1.8 M solution for human glucose tolerance test (GTT)], and their higher values reflect the lower toxicity of glucose over pyruvate. As GTT and FDG-based PET exams are usually done under fasting, the ensuing ^2H MRSI characterizations were carried out on fasted and nonfasted animals, as also detailed below. Additional experiments involved the injection of enriched [3,3′,3″-$^2H_3$]-lactate (250 μl of bolus, 130 mM, Cortecnet, Voisins-le-Bretonneux, France), as well as a slow infusion of 40 mg of the deuterated pyruvate in 500 μl of PBS (0.73 M solution).

Magnetic resonance imaging

All $^2H/^1H$ measurements were conducted on a 15.2 T Bruker scanner running Paravision 6, using 20-mm-diameter surface coils tuned to 649.93 MHz (^1H) and 99.77 MHz (^2H). To maximize the experimental sensitivity, SSFP-based ^2H CSI sequences were used (*26*, *30*), optimized for DMI with the following parameters: 2-ppm carrier frequency, repetition time TR = 11.48 ms, flip angle = 60°, 32 × 32 N_xxN_y matrices, in-plane field of view (FOV) = 40 mm by 40 mm, 20-mm slices covering the tumor areas, and 0.63-ms-long excitation pulse. These parameters align the SSFP limitations with optimal conditions for detecting chemical shifts at positions 4.7, 3.6, 2.2, and 1.2 ppm, which correspond to the physiological ^2H NMR offsets observed for the in vivo water, glucose, pyruvate, and lactate resonances, respectively. Forty-six points were sampled in the gradient-free free induction decays at 5-kHz rates; the initial four points were discarded due to corruption by the digital filtering. To increase the experimental sensitivity, weighted signal averaging of the phase-encoding domains was applied. CSI-SSFP data were thus collected with a number of averages *NA* set at 20 for the center of *k*-space, and the remaining points weighted as (*39*)

$$m(n_x, n_y) = \text{(int)}\left\{1.5 + (NA-1)\cdot 0.25\cdot\left[1+\cos\left(\frac{2\pi n_x}{N_x}\right)\right]\cdot\left[1+\cos\left(\frac{2\pi n_y}{N_y}\right)\right]\right\} \quad (1)$$

where $-\frac{N_x}{2} \le n_x \le \frac{N_x}{2} - 1$ and $-\frac{N_y}{2} \le n_y \le \frac{N_y}{2} - 1$ index the sampled points, and this Hamming weighting increases the point spread function by 1.8 over the nominal FOV/N spatial resolution. The whole *k*-space was sampled in ~30 s, using 0.2-ms-long gradient pulses in all cases. This weighted *k*-space averaging was repeated 12 identical times for the sake of signal averaging, leading to ~6 min per ^2H MRSI image. Each of these images was preceded by a nonlocalized ^2H 1D NMR spectral acquisition, whereby 256 scans were collected in ~30 s with 5-kHz spectral widths. These alternated imaging/spectroscopic acquisitions were continued for a few hours; both sets of data are presented below.

In addition to ^2H acquisitions, ^1H coronal images were collected using TurboRARE: 10 slices, 0.8-mm thickness, with the same in-plane FOV as in the ^2H MRSI experiments, and a 512 × 512 encoding matrix. ^1H B_0 maps were obtained throughout the ^2H MRSI scans using a 3D double-gradient echo, with the same FOVs as for DMI and a 64 × 64 × 8 encoding matrix. These were then included in the CSI-SSFP reconstruction process.

The ^2H images were reconstructed by zero-filling to 64 × 64 points, 2D Fourier transform, and the combined chemical shift/metabolic kinetic separation "RK-SpecRecon" described in (*36*). By relying on the a priori known chemical shifts of the different sites and on the ^1H-based acquisitions providing B_0 field inhomogeneity maps, this provided spectrally resolved images for the different metabolites, with limits of detection for the lactate methyl peak in the 0.1 to 0.2 mM range. Metabolic concentrations were computed assuming ~10 mM concentrations of HDO before the injections and took into account the SSFP scanning parameters and the T_1/T_2 for each species. As HDO in the tumor could exhibit longer T_2 values than in healthy tissues, leading to an increase in their SSFP signal intensities, HDO concentrations throughout the targeted FOV were normalized to equal pre-injection values, thereby accounting to some extent for potential T_2 heterogeneities.

Supplementary Materials

This PDF file includes:

Supplementary Text
Figs. S1 to S9

REFERENCES AND NOTES

1. S. M. Ametamey, M. Honer, P. A. Schubiger, Molecular imaging with PET. *Chem. Rev.* **108**, 1501–1516 (2008).
2. O. Warburg, F. Wind, E. Negelein, The metabolism of tumors in the body. *J. Gen. Physiol.* **8**, 519–530 (1927).
3. O. Warburg, On the origin of cancer cells. *Science* **123**, 309–314 (1956).
4. F. A. Gallagher, An introduction to functional and molecular imaging with MRI. *Clin. Radiol.* **65**, 557–566 (2010).
5. K. Golman, R. I. Zandt, M. Thaning, Real-time metabolic imaging. *Proc. Natl. Acad. Sci. U.S.A.* **103**, 11270–11275 (2006).
6. J. Kurhanewicz, D. B. Vigneron, J. H. Ardenkjaer-Larsen, J. A. Bankson, K. Brindle, C. H. Cunningham, F. A. Gallagher, K. R. Keshari, A. Kjaer, C. Laustsen, D. A. Mankoff, M. E. Merritt, S. J. Nelson, J. M. Pauly, P. Lee, S. Ronen, D. J. Tyler, S. S. Rajan, D. M. Spielman, L. Wald, X. Zhang, C. R. Malloy, R. Rizi, Hyperpolarized 13C MRI: Path to clinical translation in oncology. *Neoplasia* **21**, 1–16 (2019).
7. T. R. Brown, B. M. Kincaid, K. Ugurbil, NMR chemical shift imaging in three dimensions. *Proc. Natl. Acad. Sci. U.S.A.* **79**, 3523–3526 (1982).
8. D. Mayer, Y. F. Yen, J. Tropp, A. Pfefferbaum, R. E. Hurd, D. M. Spielman, Application of subsecond spiral chemical shift imaging to real-time multislice metabolic imaging of the rat in vivo after injection of hyperpolarized 13C1-pyruvate. *Magn. Reson. Med.* **62**, 557–564 (2009).
9. M. Vaeggemose, R. F. Schulte, C. Laustsen, Comprehensive literature review of hyperpolarized Carbon-13 MRI: The road to clinical application. *Metabolites* **11**, 219 (2021).
10. Z. J. Wang, M. A. Ohliger, P. E. Z. Larson, J. W. Gordon, R. A. Bok, J. Slater, J. E. Villanueva-Meyer, C. P. Hess, J. Kurhanewicz, D. B. Vigneron, Hyperpolarized13C MRI: State of the art and future directions. *Radiology* **291**, 273–284 (2019).
11. E. Cavallari, C. Carrera, M. Sorge, G. Bonne, A. Muchir, S. Aime, F. Reineri, The 13C hyperpolarized pyruvate generated by para-Hydrogen detects the response of the heart to altered metabolism in real time. *Sci. Rep.* **8**, 8366 (2018).
12. K. W. Chan, M. T. McMahon, Y. Kato, G. Liu, J. W. Bulte, Z. M. Bhujwalla, D. Artemov, P. C. van Zijl, Natural D-glucose as a biodegradable MRI contrast agent for detecting cancer. *Magn. Reson. Med.* **68**, 1764–1773 (2012).
13. F. A. Nasrallah, G. Pagès, P. W. Kuchel, X. Golay, K. H. Chuang, Imaging brain deoxyglucose uptake and metabolism by glucoCEST MRI. *J. Cereb. Blood Flow Metab.* **33**, 1270–1278 (2013).
14. J. C. M. Low, A. J. Wright, F. Hesse, J. Cao, K. M. Brindle, Metabolic imaging with deuterium labeled substrates. *Prog. Nucl. Magn. Reson. Spectrosc.* **134–135**, 39–51 (2023).
15. M. Lu, X. H. Zhu, Y. Zhang, G. Mateescu, W. Chen, Quantitative assessment of brain glucose metabolic rates using in vivo deuterium magnetic resonance spectroscopy. *J. Cereb. Blood Flow Metab.* **37**, 3518–3530 (2017).
16. H. M. de Feyter, K. L. Behar, Z. A. Corbin, R. K. Fulbright, P. B. Brown, S. McIntyre, T. W. Nixon, D. L. Rothman, R. A. de Graaf, Deuterium metabolic imaging (DMI) for MRI-based 3D mapping of metabolism in vivo. *Sci. Adv.* **4**, eaat7314 (2018).
17. F. Kreis, A. J. Wright, F. Hesse, M. Fala, D. Hu, K. M. Brindle, Measuring tumor glycolytic flux in vivo by using fast deuterium MRI. *Radiology* **294**, 289–296 (2020).
18. H. M. De Feyter, R. A. de Graaf, Deuterium metabolic imaging–Back to the future. *J. Magn. Reason.* **326**, 106932 (2021).
19. American Cancer Society, "Key statistics for pancreatic cancer" (February 11, 2019); https://cancer.org/cancer/types/pancreatic-cancer/about/key-statistics.html) [the easiest access to this source is via the URL].
20. C. Wallis, Why pancreatic cancer is on the rise (Scientific American, 2018; https://scientificamerican.com/article/why-pancreatic-cancer-is-on-the-rise/) [the easiest access to this source is via the URL]. p. 24.
21. E. S. Lee, J. M. Lee, Imaging diagnosis of pancreatic cancer: A state-of-the-art review. *World J. Gastroenterol.* **20**, 7864–7877 (2014).
22. E. M. Serrao, M. I. Kettunen, T. B. Rodrigues, P. Dzien, A. J. Wright, A. Gopinathan, F. A. Gallagher, D. Y. Lewis, K. K. Frese, J. Almeida, W. J. Howat, D. A. Tuveson, K. M. Brindle, MRI with hyperpolarised [1-13C]pyruvate detects advanced pancreatic preneoplasia prior to invasive disease in a mouse model. *Gut* **65**, 465–475 (2016).
23. R. P. Martinho, Q. Bao, S. Markovic, D. Preise, K. Sasson, L. Agemy, A. Scherz, L. Frydman, Identification of variable stages in murine pancreatic tumors by a multiparametric approach employing hyperpolarized13C MRSI,1H diffusivity and1H T1MRI. *NMR Biomed.* **34**, e4446 (2021).
24. H. Stødkilde-Jørgensen, C. Laustsen, E. S. S. Hansen, R. Schulte, J. H. Ardenkjaer-Larsen, A. Comment, J. Frøkiær, S. Ringgaard, L. B. Bertelsen, M. Ladekarl, B. Weber, Pilot study experiences with hyperpolarized [1-13c]pyruvate mri in pancreatic cancer patients. *J. Magn. Reson. Imaging* **51**, 961–963 (2020).
25. S. Markovic, T. Roussel, L. Agemy, K. Sasson, D. Preise, A. Scherz, L. Frydman, Deuterium MRSI characterizations of glucose metabolism in orthotopic pancreatic cancer mouse models. *NMR Biomed.* **34**, e4569 (2021).
26. D. C. Peters, S. Markovic, Q. Bao, D. Preise, K. Sasson, L. Agemy, A. Scherz, L. Frydman, Improving deuterium metabolic imaging (DMI) signal-to-noise ratio by spectroscopic multi-echo bSSFP: A pancreatic cancer investigation. *Magn. Reson. Med.* **86**, 2604–2617 (2021).
27. E. T. Montrazi, K. Sasson, L. Agemy, D. C. Peters, O. Brenner, A. Scherz, L. Frydman, High-sensitivity deuterium metabolic MRI differentiates acute pancreatitis from pancreatic cancers in murine models. *Sci. Rep.* **13**, 19998 (2023).
28. G. Batsios, C. Taglang, M. Tran, N. Stevers, C. Barger, A. M. Gillespie, S. M. Ronen, J. F. Costello, P. Viswanath, Deuterium metabolic imaging reports on TERT expression and early response to therapy in cancer. *Clin. Cancer Res.* **28**, 3526–3536 (2022).
29. T. Harris, G. Eliyahu, L. Frydman, H. Degani, Kinetics of hyperpolarized $^{13}C_1$-pyruvate transport and metabolism in living human breast cancer cells. *Proc. Natl. Acad. Sci. U.S.A.* **106**, 18131–18136 (2009).
30. Y. Rao, S. Gammon, N. M. Zacharias, T. Liu, T. Salzillo, Y. Xi, J. Wang, P. Bhattacharya, D. Piwnica-Worms, Hyperpolarized [1-13C]pyruvate-to-[1-13C]lactate conversion is rate-limited by monocarboxylate transporter-1 in the plasma membrane. *Proc. Natl. Acad. Sci. U.S.A.* **117**, 22378–22389 (2020).
31. T. Harris, H. Degani, L. Frydman, Hyperpolarized ^{13}C NMR studies of glucose metabolism in living breast cancer cell cultures. *NMR Biomed.* **26**, 1831–1843 (2013).
32. T. B. Rodrigues, E. M. Serrao, B. W. C. Kennedy, D. Hu, M. I. Kettunen, K. M. Brindle, Magnetic resonance imaging of tumor glycolysis using hyperpolarized ^{13}C-labeled glucose. *Nat. Med.* **20**, 93–97 (2014).
33. E. E. Kim, S. K. Chung, T. P. Haynie, C. G. Kim, B. J. Cho, D. A. Podoloff, R. S. Tilbury, D. J. Yang, W. K. Yung, R. P. Moser Jr., Differentiation of residual or recurrent tumors from post-treatment changes with F-18 FDG PET. *Radiographics* **12**, 269–279 (1992).
34. E. Goshen, T. Davidson, S. T. Zwas, D. Aderka, PET/CT in the evaluation of response to treatment of liver metastases from colorectal cancer with bevacizumab and irinotecan. *Technol. Cancer Res. Treat.* **5**, 37–43 (2006).
35. M. S. Hofman, R. J. Hicks, How we read oncologic FDG PET/CT. *Cancer Imaging* **16**, 35 (2016).
36. E. T. Montrazi, Q. Bao, R. P. Martinho, D. C. Peters, T. Harris, K. Sasson, L. Agemy, A. Scherz, L. Frydman, Deuterium imaging of the Warburg effect at sub-millimolar concentrations by joint processing of the kinetic and spectral dimensions. *NMR Biomed.* **36**, e4995 (2023).
37. J. Li, W. Qian, T. Qin, Y. Xiao, L. Cheng, J. Cao, X. Chen, Q. Ma, Z. Wu, Mouse-Derived allografts: A complementary model to the KPC mice on researching pancreatic cancer in vivo. *Comput. Struct. Biotechnol. J.* **17**, 498–506 (2019).
38. M. J. Albers, R. Bok, A. P. Chen, C. H. Cunningham, M. L. Zierhut, V. Y. Zhang, S. J. Kohler, J. Tropp, R. E. Hurd, Y.-F. Yen, S. J. Nelson, D. B. Vigneron, J. Kurhanewicz, Hyperpolarized 13C lactate, pyruvate, and alanine: Noninvasive biomarkers for prostate cancer detection and grading. *Cancer Res.* **68**, 8607–8615 (2008).
39. A. Greiser, M. von Kienlin, Efficient k-space sampling by density-weighted phase-encoding. *Magn. Reson. Med.* **50**, 1266–1275 (2003).

Acknowledgments: We are grateful to T. Harris and H,. Allouche-Arnon for experimental assistance and council and to V. Frydman for the preparation of the deuterated sodium pyruvate. **Funding:** This work was supported by the Minerva Foundation (L.F.), the Israel Science Foundation (L.F.) grant nos. 3594/21 and 1874/22, and the Israel Cancer Research Foundations (L.F.), as well as by the Israel Ministry of Science (L.F.). L.F. heads the Clore Institute for High-Field Magnetic Resonance Imaging and Spectroscopy, whose support is also acknowledged. **Author contributions:** E.T.M. and L.F. designed research; E.T.M. performed the experiments; K.S., L.A., and A.S. contributed tools; E.T.M. and L.F. analyzed data; E.T.M. and L.F. wrote the paper. **Competing interests:** The authors declare that they have no competing interests. **Data and materials availability:** All data needed to evaluate the conclusions in the paper are present in the paper and/or the Supplementary Materials.

Submitted 9 November 2023
Accepted 7 February 2024
Published 13 March 2024
10.1126/sciadv.adm8600